Atmospheric
Measurement
Techniques
Open Access
EGU
Discussions

Tracking aerosols and SO$_2$ clouds from the Raikoke eruption: 3D view from satellite observations

Nick Gorkavyi [1], Nickolay Krotkov [2], Can Li [3], Leslie Lait [1], Peter Colarco [2], Simon Carn[4], Matthew
DeLand [1], Paul Newman [2], Mark Schoeberl[5], Ghassan Taha[2,6], Omar Torres[2], Alexander Vasilkov[1],
Joanna Joiner [2]

[1] Science Systems and Applications, Lanham, MD, USA
[2] NASA, Goddard Space Flight Center, Greenbelt, MD, USA
[3] University of Maryland, College Park, MD, USA
[4] Michigan Technological University, Houghton, MI, USA
[5] Science and Technology Corporation, Columbia, MD, USA
[6] USRA, Greenbelt, MD, USA

Correspondence: Nick Gorkavyi (nick.gorkavyi@ssaihq.com)

Abstract. The June 21, 2019 eruption of the Raikoke volcano (Kuril Islands, Russia, 48°N, 153°E) produced significant amounts of volcanic aerosols (sulfate and ash) and sulfur dioxide (SO$_2$) gas that penetrated into the lower stratosphere. The dispersed SO$_2$ and sulfate aerosols in the stratosphere were still detectable by multiple satellite sensors for three months after the eruption. For this study of SO$_2$ and aerosol clouds we use data obtained from two of the Ozone Mapping Profiler Suite (OMPS) sensors on the Suomi National Polar-orbiting Partnership (SNPP) satellite: total column SO$_2$ from the Nadir Mapper (NM) and aerosol extinction profiles from the Limb Profiler (LP) as well as other satellite data sets. The LP standard aerosol extinction product at 674 nm has been re-processed with an adjustment correcting for limb viewing geometry effects. It was shown that the amount of SO$_2$ decreases with a characteristic period of 8-18 days and the peak of sulfate aerosol recorded at a wavelength of 674 nm lags the initial peak of SO$_2$ by 1.5 months. Using satellite observations and a trajectory model, we examined the dynamics of unusual atmospheric feature that was observed, a stratospheric coherent circular cloud (CCC) of SO$_2$ and aerosol from July 18 to September 22, 2019.
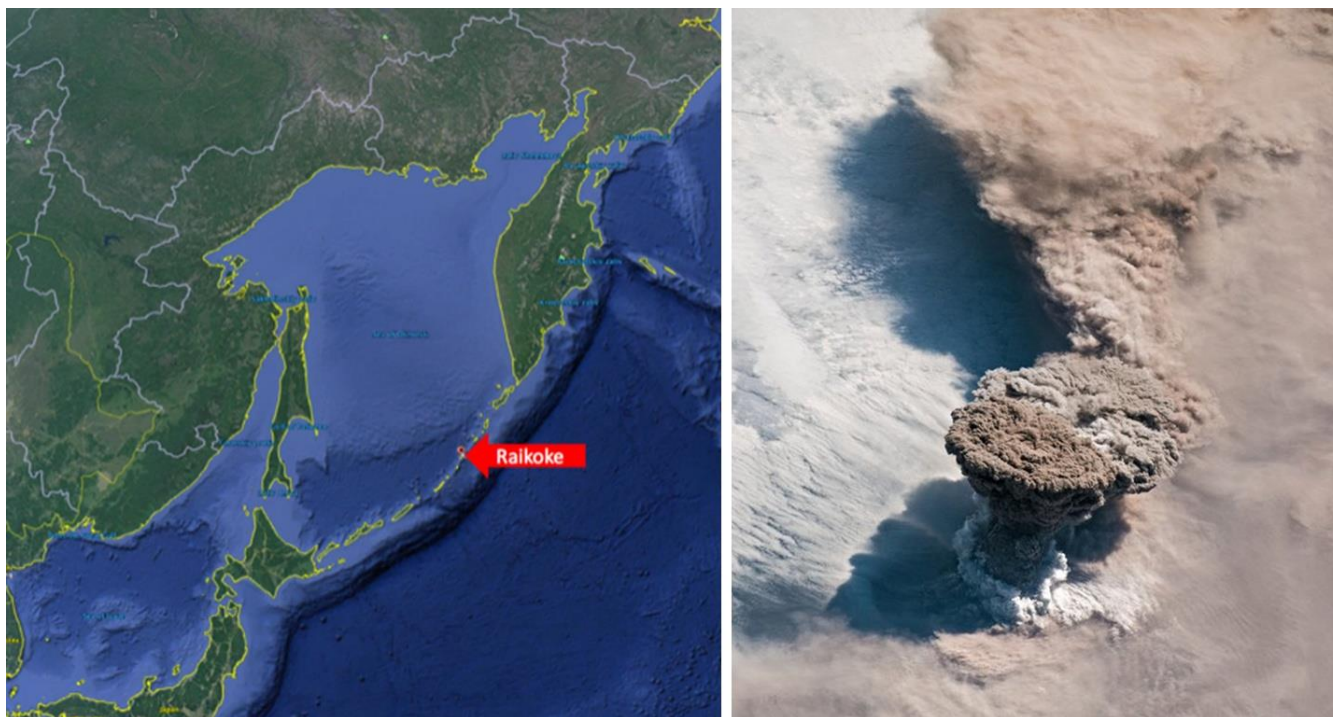
1 Introduction

An eruption of the Raikoke volcano (See Fig. 1, 0.55 km altitude, uninhabited island at 48.29°N, 153.4°E) occurred on June 21, 2019 at 6 p.m. UT. The eruption was so strong that a cloud of ash and volcanic gases was ejected to a height of 17-19 km, putting a significant part of the Raikoke volcanic plume into the stratosphere and above the heights of clouds and the tropopause, which is ~ 10-12 km for such northern latitudes (see Fig. 1). The Microwave Limb Sounder (MLS) data for June 23-27, 2019 show that the observed parts of the SO$_2$ cloud had a height of 11 to 18 km, with a peak concentration at 14 km. The maximum volcanic cloud top height rises more than 6 km within 4 days after the eruption due to aerosol–radiation interaction (Muser et al., 2020).

The study of volcanic plumes and the transformation of their SO$_2$ into aerosols is interesting for several reasons. Firstly, clouds of ash and sulfate aerosol are aviation hazards. Secondly, the lifetime of SO$_2$ depends on its injection height, total mass, dispersion pattern and the concentrations of oxidants that vary with season and location (Krotkov et al., 2010). SO$_2$ from volcanic eruptions has a longer lifetime if it is injected into the stratosphere. SO$_2$ in the stratosphere is converted to sulfate aerosol, which interacts with the long-lived Junge layer—the naturally occurring background stratospheric aerosol layer. Further, the dynamics of the Junge layer itself is not well understood. In addition, stratospheric aerosols are an important factor for climate forcing because aerosols modify both the shortwave and longwave radiation in the atmosphere and reaching the Earth's surface (Toohey et al., 2019; von Savigny et al., 2020). Thus, each case of volcanic injection of

large amounts of SO_2 into the stratosphere is of great interest from the point of view of Earth sciences. Our ability to study volcanic clouds and their impacts has evolved in recent decades along with satellite technology (Bovensmann et al., 1999; Carn et al., 2003, 2007, 2008, 2009, 2017; Penning de Vries et al., 2014; Sandvik et al., 2019; Hedelt et al., 2019; Theys et al., 2019; Fisher et al., 2019). The spectral data obtained from satellites has made it possible to analyze in detail volcanic eruptions, such as of the Pinatubo (Bluth et al., 1992) and Kasatochi (Bourassa et al., 2010; Krotkov et al., 2010).

Figure 1: Left: Raikoke volcano (Kuril Islands, Russia, 48ᵒN, 153ᵒE) (Google Maps, Imagery: NASA; Map data: SK telecom)). Right: photo of the Raikoke eruption (06/21/2019), which shows that the volcanic plume rose much higher than the layer of tropospheric clouds (Photo: iss059e119250 June 22, 2019, ISS/NASA, https://visibleearth.nasa.gov/images/145226/raikoke-erupts/145230w)

The 2019 eruption of Raikoke was well observed by a number of satellite sensors, for example, the Ozone Monitoring Instrument (OMI), the Tropospheric Monitoring Instrument (TROPOMI), the Ozone Mapping Profiler Suite (OMPS) Nadir Mapper (NM) and Limb Profiler (LP) and the Cloud-Aerosol Lidar with Orthogonal Polarization (CALIOP). Studying the nadir data of OMPS NM and TROPOMI, our attention was drawn to an interesting phenomenon in the presence of compact stratospheric SO_2 clouds, hereafter referred to as coherent circular clouds or CCC, each about 300 km in diameter: the first noted on June 29, 2019 centered at 52°N, 157°W (near Alaska) and the second observed starting on July 21, 2019 centered at 46.5°N, 167°E (near Kamchatka). The first of these moved towards the North Pole while the second moved to ~ 30°N, where it remained for more than two months, having made almost three complete revolutions around the Earth.

A dense cloud of SO_2 and aerosol that formed after the eruption of the Raikoke volcano spread over a week at latitudes above 40°N (see TROPOMI SO_2 map on June 29, 2019 in Fig. 2). Atmospheric currents stretched the cloud into long jets, twisted them with spirals and even formed CCCs, as shown in Fig. 2 in the region near the coordinates 52°N, 156°W. To analyze in detail the evolution and dynamics of the Raikoke volcanic cloud, we examine 1) the amount of SO_2 and aerosol emitted during the eruption using nadir and limb data; 2) the mutual evolution of SO_2 and aerosol for 100 days, starting from

the moment of the eruption with an adjustment correcting for limb viewing geometry effects; 3) the propagation of the CCCs with a case study near the end of July 2019 using a trajectory model.

70
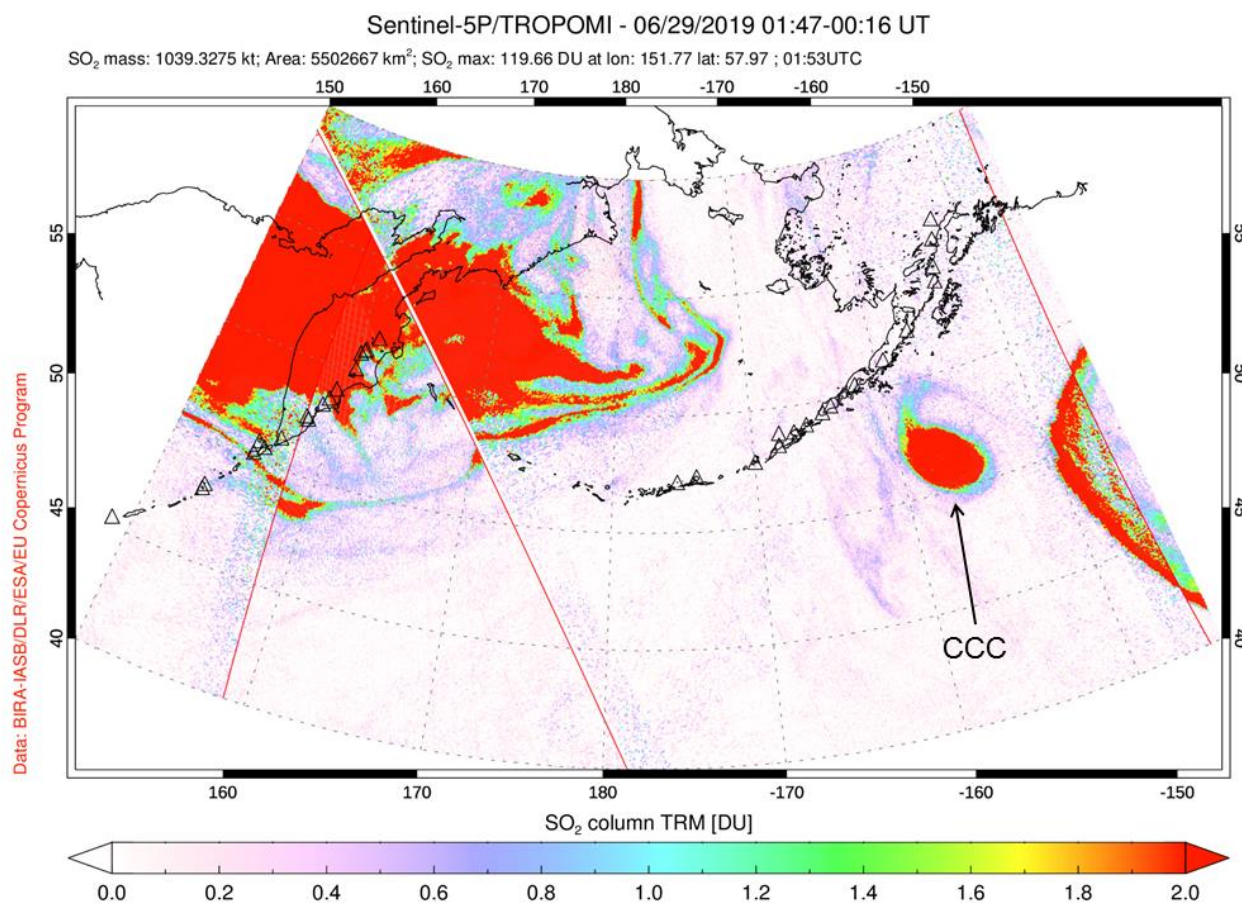
Figure 2: TROPOMI image of SO$_2$ clouds, a week after the Raikoke eruption (Image: courtesy Copernicus TROPOMI/Sentinel-5Precursor SO$_2$ data, https://so2.gsfc.nasa.gov/). The triangles represent the location of the volcanoes.

2 Data and Methods

In this section, we detail the instruments and methods used to 1) Examine SO$_2$ and aerosol distributions obtained from nadir for SO$_2$ and limb and lidar for aerosol; 2) calculate of zonal mean values of SO$_2$ and aerosol as a function of a height using nadir data for SO$_2$ and limb data for aerosol; 3) employ trajectory modeling for analysis of individual clouds.

Atmospheric
Measurement
Techniques
Discussions

Open Access

EGU

2.1 Satellite Mapping of SO$_2$

85

We use SO$_2$ total column data obtained by two satellite spectrometers: 1) TROPOMI (see Fig. 2, Theys et al., 2017, 2019) on the Sentinel 5 precursor satellite and OMPS Nadir Mapper (NM) on the Suomi National Polar-orbiting Partnership, SNPP, satellite (Li et al., 2013, 2015; Zhang et al., 2017). Both instruments observe the Earth's backscatter radiance and solar irradiance from visible through ultraviolet wavelengths with two-dimensional charge-coupled devices (CCDs), measuring in

90 the spectral domain in one dimension and in the spatial domain (across a satellite track) in the other dimension. The satellite motion provides measurements along the satellite track. The spatial resolution of TROPOMI (3.5 km by 7 km) is much finer than that from OMPS measurements made in the nominal mode (50 km by 50 km) and the spectral resolution is higher for TROPOMI as well (~ 0.5 nm as compared with ~ 1 nm for OMPS). The satellite swaths are wide (2700 km for TROPOMI and 2800 km for OMPS), providing nearly daily global coverage. SO$_2$ is retrieved with backscatter solar spectral

95 measurements at ultraviolet wavelengths (312-390 nm). TROPOMI uses a spectral fitting algorithm based on differential optical absorption spectroscopy (DOAS) (Theys et al., 2017, 2019). OMPS uses spectral fitting approach with a principal component analysis (PCA) scheme (Li et al., 2013).

2.2 Aerosol profile data

100

We use aerosol data from CALIOP (Fairlie et al., 2014) and OMPS LP (Loughman et al., 2018; Chen et al., 2018). The height of an aerosol cloud can be estimated with both OMPS LP and CALIOP. We use the CALIOP lidar images for aerosol, specifically 532 nm total attenuated backscatter signal with a spatial resolution of 40 km along track and a vertical resolution of 120 m (altitude < 20 km) and 360 m (altitude > 20 km).

105

OMPS LP hyperspectral measurements capture aerosol data with a sampling of ~1 km in altitude. OMPS LP views the atmosphere in a backward direction along the orbit track with three vertical slits, one (central) aligned with the orbit track and the other two (left and right) separated by ±4.25° horizontally. Here, we use data from version 1.5 (Chen et al., 2018).

110 Limb measurements of the atmosphere that view an altitude H at the tangent point also view altitudes above H in the foreground and background of the line of sight. However, the converse situation is also true: an object at a fixed altitude H will appear to be at a lower altitude h if it is located closer or farther than the tangent point. This is shown schematically in Fig. 3, where a single cloud is located at true altitude H and 5 successive LP measurement events (each event generates a new profile) are illustrated. For event C, the cloud location is at the tangent point, and the apparent altitude h equals the true

115 altitude H. For events A and B, the cloud position is closer to the LP instrument than the tangent point, and h is less than H. For events D and E, the cloud position is farther from the LP instrument than the tangent point, and again $h < H$.

Plotting successive altitude profiles of LP signal strength (e.g., extinction coefficient) when a vertically limited feature (such as a cloud) is present gives the impression of an "arch" in the data. Figure 4, where extinction values are color-coded for

120 intensity, and a lower threshold of $1x10^{-3}$ km^{-1} is applied, illustrates this effect. The maximum values (yellow) appear to vary in altitude by 2-3 km due to the projection effect shown in Fig. 3. Note that this effect will be present for high, thin clouds such as cirrus clouds as well as for aerosol plumes. If we believe that these lower altitude values do not represent a true aerosol signal, we need to apply a correction in order to accurately determine overall aerosol loading.

Atmospheric
Measurement
Techniques
Discussions
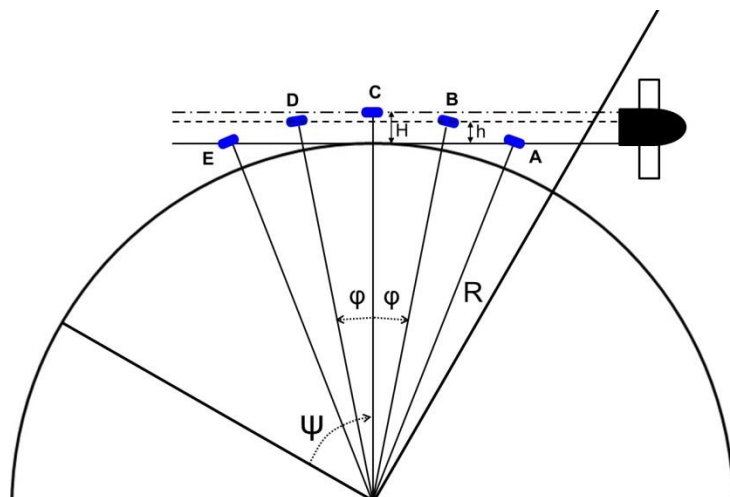
Figure 3: The diagram for observations of the limb sensor, showing the relationship between the observed (h) and real (H) heights of five clouds, as well as φ - angular displacement of the position of the clouds.

The relationship between true cloud height H and apparent cloud height h in Figure 3 is given by a simple function (DeLand and Gorkavyi, 2021):

$$\cos \varphi \; = \; \frac{R+h}{R+H} \qquad\qquad (1)$$

where R is the radius of the Earth; φ is the angular displacement. Table 1 gives some specific examples of the angular displacement predicted for specific combinations of H and h. This displacement is approximately equal to a shift in latitude for a sun-synchronous satellite such as S-NPP (inclination = 98.9°) outside the polar regions. From this table, we see that for a true cloud at $H = 25$ km, the apparent cloud signal at h = 15 km would be displaced by ~3.2° both earlier and later along the orbit. This total separation of ~6.4° is consistent with the "arch width" at 15 km shown in Fig. 4. Note also that because of differences in overall path length, we expect events A and B in Fig. 3 (left branch of "arch" in Fig. 4) to have a stronger signal than the corresponding events D and E at the same apparent altitude. We can therefore use Eq. (1) to calculate and apply a correction for determining the magnitude and position of an aerosol cloud.

Table 1. The visible height h and angular displacement φ for the cloud with real height H.

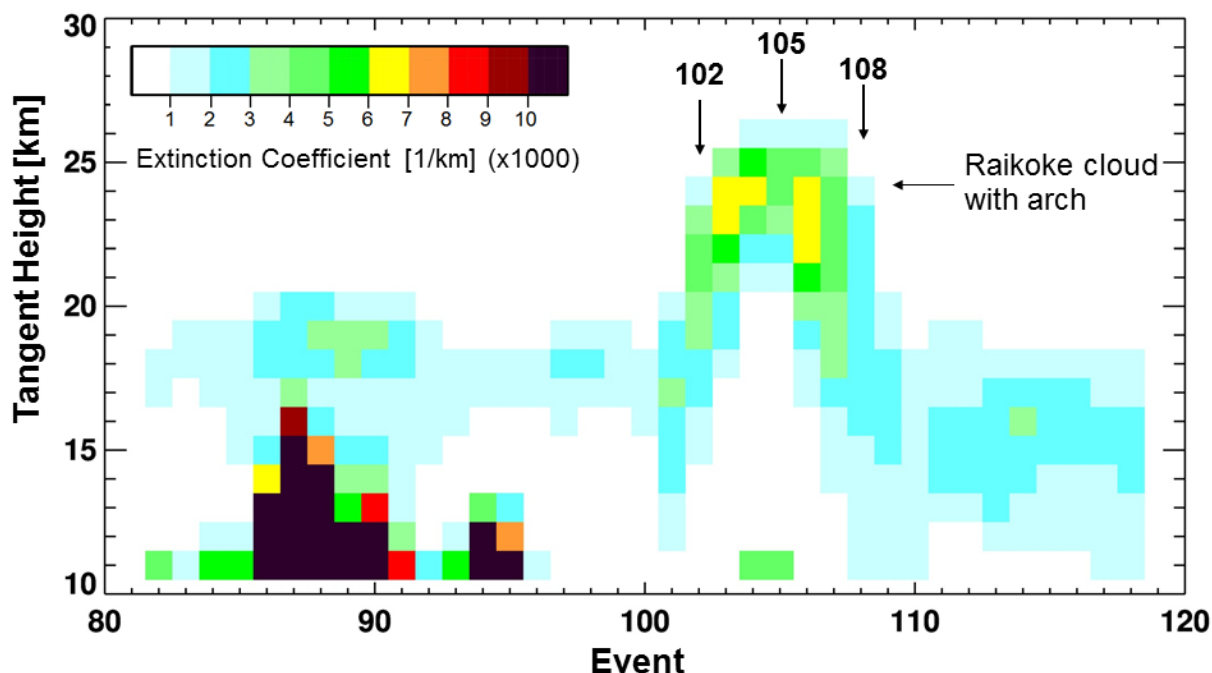| $h\backslash H$	$H = 10$ km	15 km	20 km	25 km	30 km
$h = 0$ km	$\varphi = 3.21°$	3.93°	4.53°	5.07°	5.55°
5 km	2.27°	3.21°	3.93°	4.53°	5.07°
10 km	-	2.27°	3.21°	3.92°	4.53°
15 km	-	-	2.27°	3.20°	3.92°
20 km	-	-	-	2.27°	3.20°
25 km	-	-	-	-	2.26°

Figure 4: The extinction coefficient profiles (674 nm) from OMPS LP for the orbit 40636 (central slit, same orbit as in Fig. 6, which shows the profiles for events 102, 105, 108) for August 31, 2019. For accurately calculating the extinction coefficient it is necessary to take into account the arch effect, which is clearly visible (OMPS LP data).

150　The arch in Fig. 4 is formed by several measurements of one CCC, which has a height of 23-25 km (see the analysis of this CCC in Sect. 3.2). Parts of the arch (between events 101 and 109) below 23 km are artifacts of multiple registrations of the same object and should be removed when calculating the total amount of aerosol at given latitudes or heights. The aerosol layer at an altitude of 18-20 km with a decrease to the north to 15-16 km is the Junge layer. It merges in frames 101-109 with a volcanic cloud arch that partially shields the Junge layer in frames 103-106. The tropical cloud in frame 88 is up to 16 km
155　altitude.

The principle of our posterior algorithm for neutralizing the "arch effect" is as follows: the data in the uppermost pixel of the arch are considered real. For a given pixel, artifact densities are calculated in pixels in the side branches of the arch. These artifact densities are subtracted from the initial arch density. The procedure is repeated for the second highest pixel in the
160　already modified arch image. This continues until the side branches of the arch completely disappear. The top pixels with the corrected density are summed into the cloud with the cleaned data.

The arch effect is a specific example of the effects of inhomogeneity along the line of sight that is an issue for all types of limb sounders. One way to account for such effects is to use a radiative transfer scheme that is able to model such effects and
165　then to use multiple observations in a tomographic retrieval (e.g., Livesay et al., 2006; Zawanda et al., 2018). Such an approach with OMPS LP aerosol profiles was discussed by Loughman et al. (2018) but has not yet been implemented. Instead, we have developed a posterior adjustment method that is effective in correcting for the arch-type effects that appear with isolated features within the lines of sights for a series of observations.

170

Atmospheric
Measurement
Techniques
Discussions

2.3 The NASA ftraj trajectory model

175   The "ftraj" trajectory model from NASA's Goddard Space Flight Center Atmospheric Chemistry and Dynamics Laboratory uses a fourth-order Runge-Kutta integration scheme to track parcels isentropically, with optional diabatic adjustments (see Schoeberl and Sparling, 1995). The model is driven with winds at 1/4° horizontal resolution and spaced every six hours apart from the Goddard Earth Observing System (GEOS) forward processing system produced by the NASA Global Modeling and Assimilation Office (GMAO). Each model run was initialized with 3000 parcels distributed randomly in a cylinder of radius 150 km centered about the location of the observed cloud and stretching between the lowest and highest potential
180   temperature (θ) values of the observed cloud. Those θ values were derived by interpolating the GEOS fields to the parcels' initial longitude, latitude, altitude, and time. Both the starting and ending cloud observations extended through a range of altitudes and hence θ values.

3 Results

185   The sensitivity of the satellite data we examined is such that the aerosol cloud from the Raikoke volcano was observable for 3 months following the eruption. Thus, a synergistic study of Raikoke volcanic emissions using various satellite-based instruments provides a good opportunity to study the dynamics of volcanic cloud dispersion. For quantitative analysis, we will use 2D SO_2 vertical column density (VCD) maps obtained by OMPS NM, as well as vertical profiles of aerosol clouds that are obtained from the OMPS LP.
190

3.1 SO_2 and aerosol evolution

The retrieved Raikoke SO_2 mass increased rapidly following the dispersion of the volcanic cloud after the eruption and then exponentially decayed with an average e-folding time scale of 8-10 days. The amount of stratospheric SO_2 decreases due to
195   photochemical conversion to sulfuric acid though gas - phase reaction with the hydroxyl radical, OH. Sulfuric acid nucleates new particles and condenses onto pre-existing particles to form long-lived stratospheric sulfate aerosol. Figure 5 shows the change in the total SO_2 mass (kt) retrieved by the OMPS NM and aerosol extinction coefficient retrieved with the OMPS LP in the latitude range 45°-65°N after the Raikoke eruption. The aerosol extinction data in Fig. 5 are shown before and after removing the "arch effect". As can be seen from Fig. 5, the aerosol extinction coefficient after removing the arch effect is
200   reduced by 30-50%.

Atmospheric
Measurement
Techniques
Open Access
EGU
Discussions
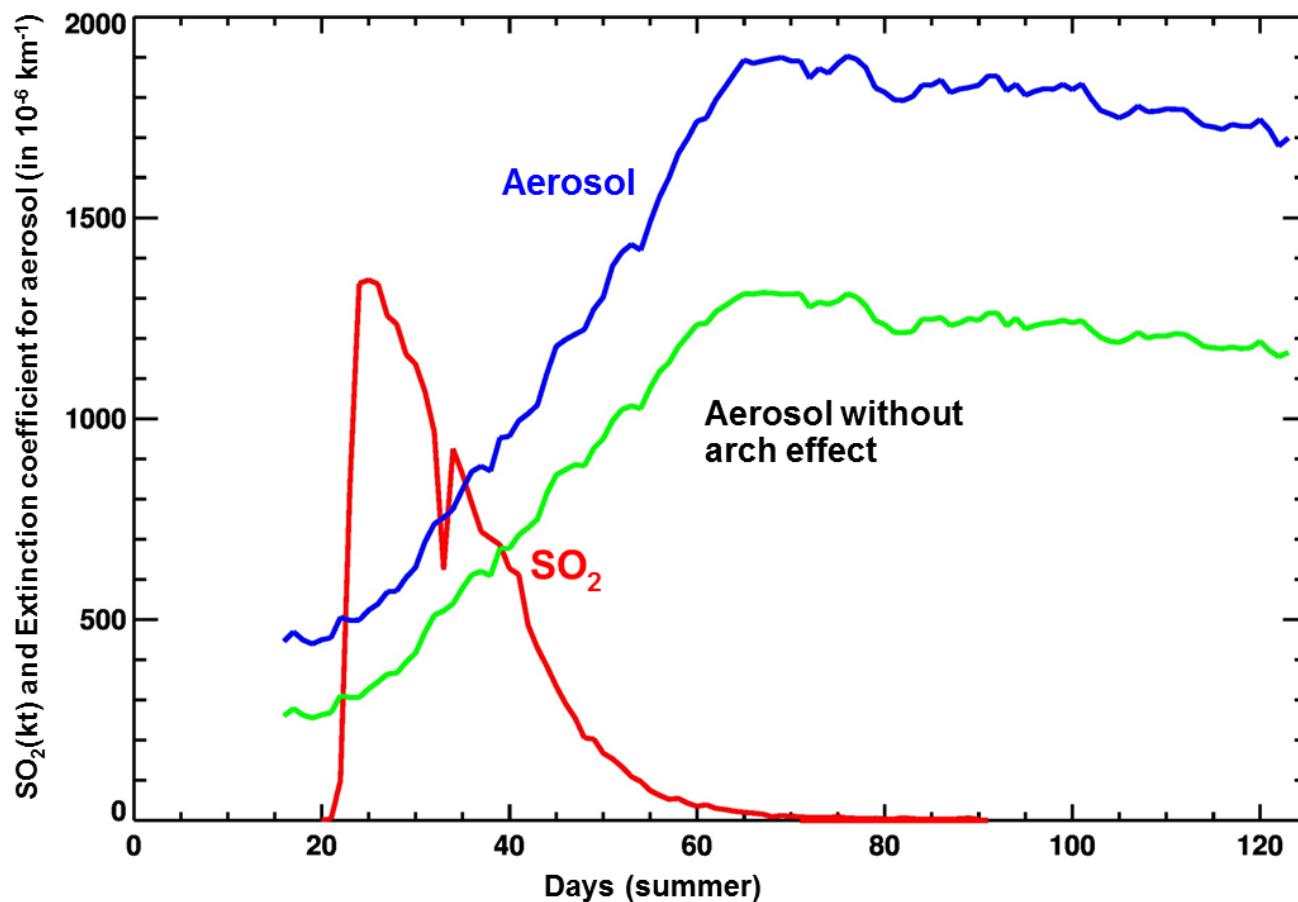
Figure 5: The daily zonal mean (45-85N) SO₂ mass (assuming a cloud height of 13 km) and the aerosol Extinction coefficient at 675 nm (13-18 km.). The retrieved SO₂ mass increases for 2 days after the eruption during rapid dispersion of the fresh opaque volcanic cloud. Following initial dispersion and fallout of ash the SO₂ mass decreases exponentially due to chemical conversion to sulfate. Aerosol extinction has opposite behavior: it increases by a factor of 4 as the concentration of SO₂ decreases, reaching a maximum ~50 days after the eruption. After that, the aerosol extinction starts to decrease due to gravitational sedimentation, but very slowly (from OMPS LP and NM data).

As can be seen from Fig. 6, the cloud SO₂ mass decreases exponentially with variable (8-18) day timescale. Aura/OMI previously measured volcanic SO₂ mass decay following the August 8, 2008 Kasatochi eruption (30°N–90°N). The overall apparent e-folding time for Raikoke is ~ 8-10 days (Fig. 6, solid black lines), in good agreement with Kasatochi e-folding time ~9 days (Krotkov et al., 2010). But there are uncertainties associated with the estimated e-folding time, as discussed below.
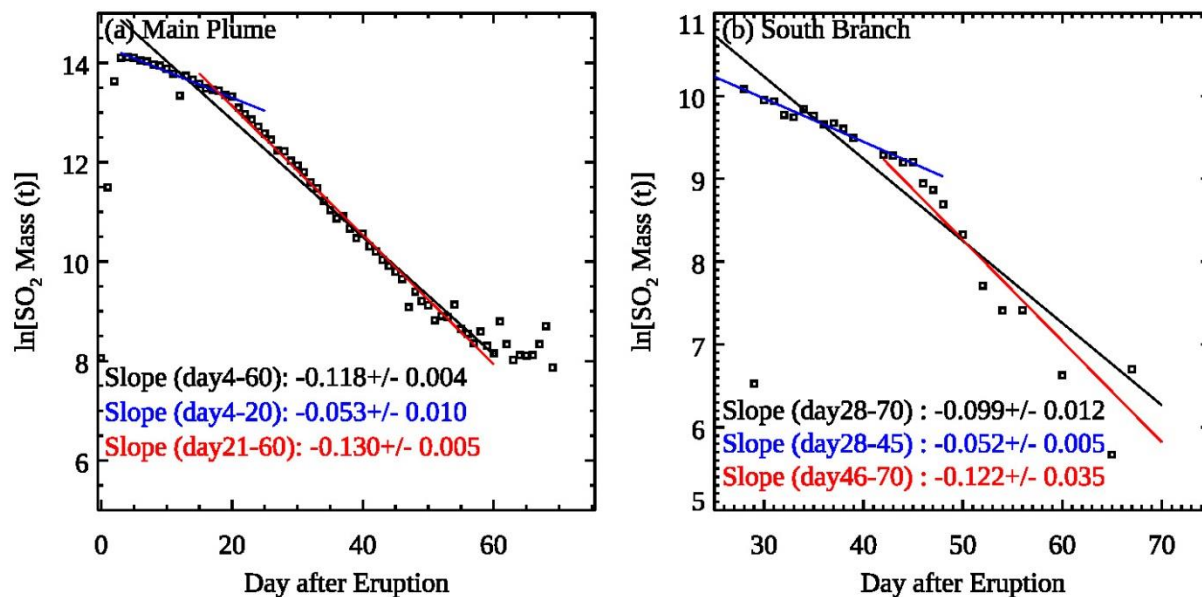
Figure 6: Time series of the logarithm of the estimated total SO$_2$ mass (in ton) within (a) the main plume and (b) the CCC to the south after the eruption. Assuming a first order loss rate for SO$_2$, the slope of the linear fit (straight line) for (a) indicates a decay rate of 0.118 day^{-1}, or an e-folding lifetime of ~8.5 days. Similarly, for (b), the decay rate is 0.099 day^{-1} and the e-folding lifetime is ~10 days. There are uncertainties in the estimated lifetime. For (a) the main plume, the estimated lifetime is ~18.9 days between 4 and 20 days after eruption, and ~7.7 days between days 21 and 60 after the eruption. For the south branch (b), the estimated lifetime is ~19.2 days between 28 and 45 days after eruption, and ~8.2 days between days 46 and 70 after the eruption.

Note that the left panel in Fig. 6 shows the following deviations from the average of the e-folding lifetime of 8.5 days: within the first 20 days after the eruption, the SO$_2$ mass falls with an apparent e-folding lifetime of 18.9 days, and between days 21 and 60, the decrease in SO$_2$ mass accelerates and the apparent e-folding lifetime is only ~8 days. The e-folding lifetime of 18.9 days, derived from the earlier stage after the eruption, probably reflects the conversion of SO$_2$ into sulfate aerosol. After that, the detection limit of the instrument becomes a more important factor, leading to faster apparent decay of the total observed SO$_2$. As the plume spreads out to larger areas, and more and more pixels with SO$_2$ fall below the detection limit of the OMPS NM sensor, the apparent decay rate becomes larger, likely reflecting the effects of both actual SO$_2$ loss and the diminished OMPS sensitivity to weaker SO$_2$ signals. Figure 6b shows a similar pattern for change in SO$_2$ in the CCC. For the period between days 28 and 45 after eruption, the e-folding lifetime is ~19 days. This suggests that the time after the eruption does not play a big role here, only the compactness of the CCC with a high level of SO$_2$ is essential. As in case Fig. 6a, the second phase of the evolution of the CCC is characterized by a faster apparent (the e-folding lifetime ~ 8 days) rate of decrease in the recorded SO$_2$.

3.2 Stratospheric aerosol from limb observations

The stratospheric aerosol optical depth shows the plume latitudinal distribution, with most of the aerosol being transported poleward (Fig. 7). Figure 7 also shows that the effects of the eruption lasted for almost a year. Increased aerosol loading in the lower stratosphere can also be attributed to two pyroCumulonimbus (pyroCb) events that took place before and after the eruption, Alberta fires (June 18) and Siberian fires (July 2) (Kloss et al., 2021). The zonal mean aerosol extinction profile

240   between 20°N and 90°N shows the vertical transport of the Raikoke plume to higher altitudes and its persistence in the lower
       stratosphere (Fig. 8). The top panel in Fig. 8 shows that the maximum altitudes of the plume are around 25 km, when the
   plume penetrates the tropics.
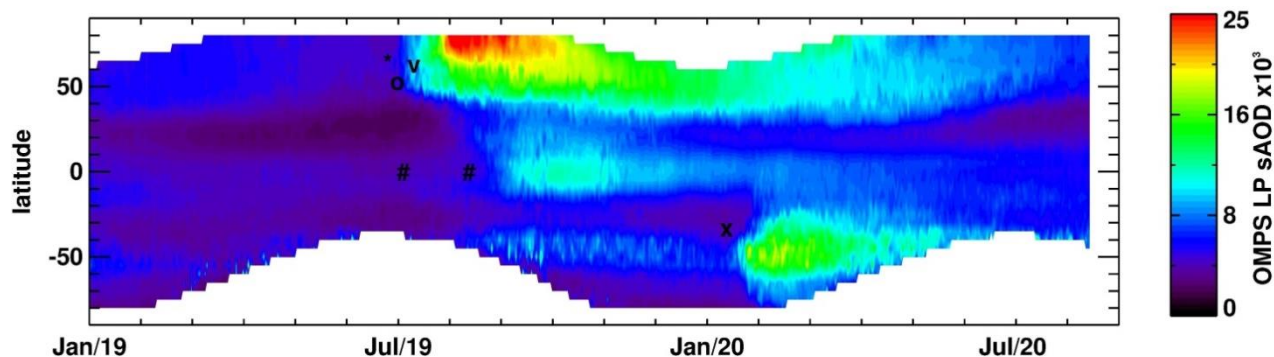
245

**Figure 7: Latitudinal distribution of the stratospheric aerosol optical depth (x 10³, sAOD) at 675 nm. "o" – Raikoke eruption, "*"
– Alberta fires, "v" – Siberian fires, "#" – Ulawun eruptions, "x" – Australian fires. The sAOD daily time series were derived by
integrating aerosol extinction profiles derived from OMPS LP above the tropopause to 35 km and averaged every five degrees of
latitude**

250
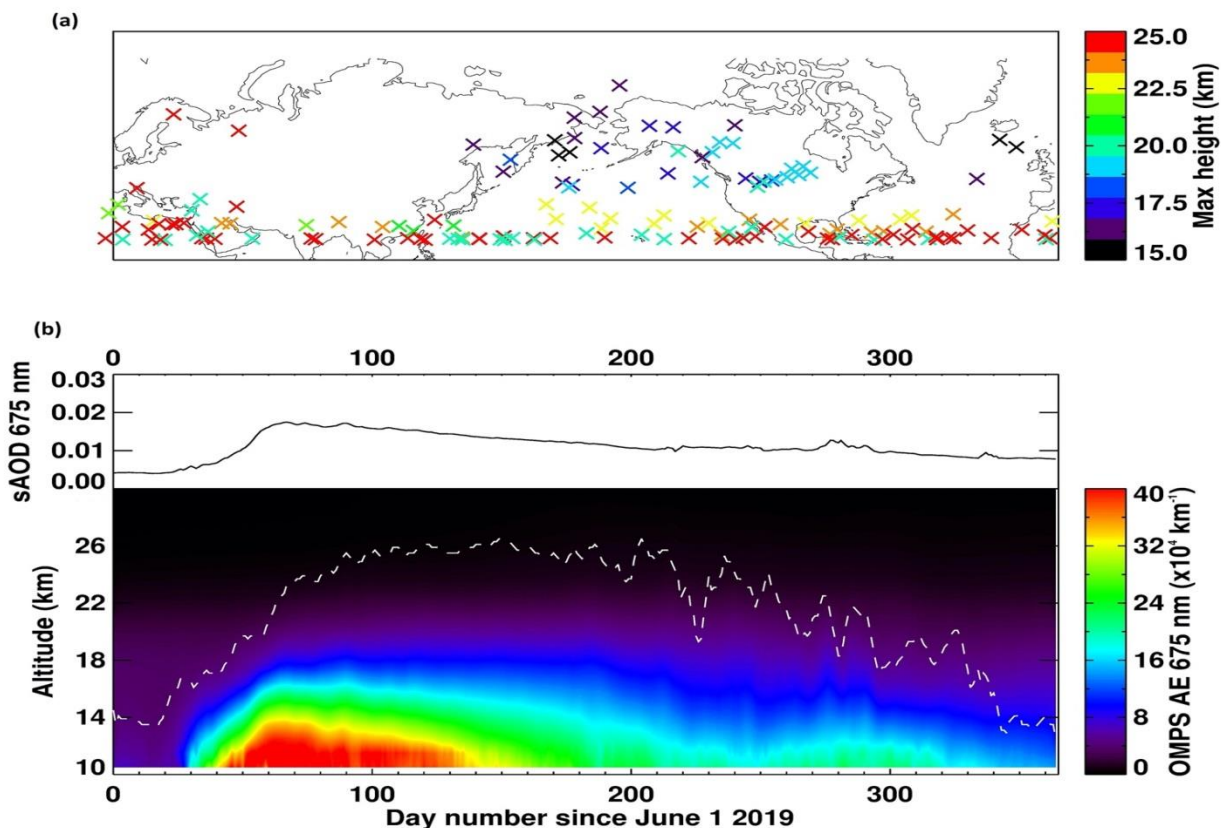
Figure 8: (a) Daily location of the maximum altitude reached by the Raikoke aerosol plume as detected by OMPS LP. The color scale shows altitude values in km. Figure 8(b): (bottom) Daily zonal mean aerosol extinction profiles at 675 nm (km^{-1}) between 20°S-90°N measured by OMPS LP from June 2019 to June 2020 and smoothed spatially using a 5 point boxcar averaging. Only profiles measured above tropopause+1 km are used. The white line is the aerosol plume maximum altitude in km.

Figure 9 shows the ratio of a daily zonal mean of the aerosol extinction coefficient for July 1 and 21 and September 1 and 30, 2019 to a similar daily zonal mean for a quiet period (June 16-20, 2019) before the eruption. The means were computed without taking into account the "arch effect" (see DeLand and Gorkavyi (2021) and Sect. 2.2). Therefore, the lower parts of the layers shown may have an overestimated extinction coefficient. In addition to increasing the density of the Junge layer (the contribution of seasonal changes is possible here), an interesting CCC appears at an altitude of about 25 km that will be discussed in Sect. 3.3.
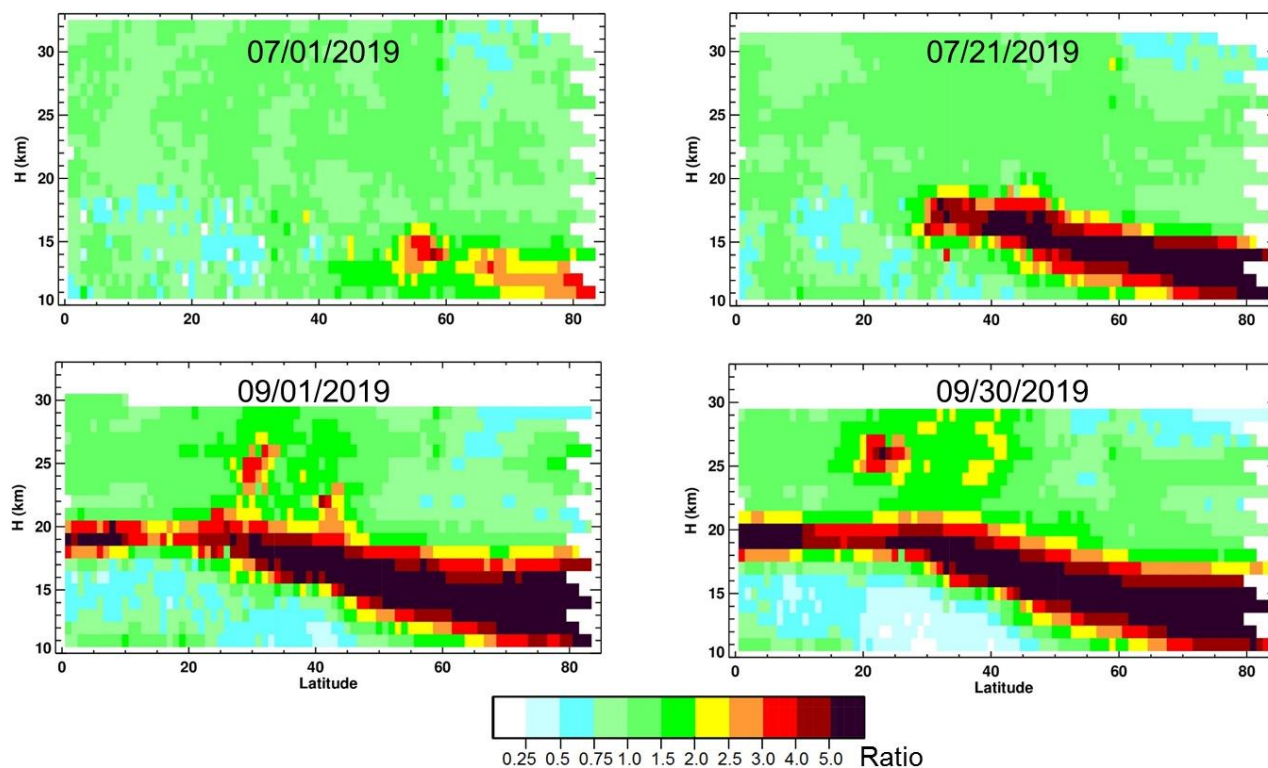
Figure 9: The ratio of the zonal mean, daily average aerosol extinction for the indicated dates after the Raikoke eruption to the averaged aerosol extinction immediately prior to the eruption shows the evolution of the volcanic aerosol in the Junge layer (13-20 km) and the occurrence of the CCC near 25 km from OMPS LP data.

Three LP aerosol extinction profiles were measured by OMPS LP on 31 August 2019, more than two months after the Raikoke eruption (Fig. 10). The extinction peak at 22-25 km represents the continued signal of the stratospheric plume from the eruption. The apparent altitude variation between these peaks also shows the impact of the LP viewing geometry on the retrieved extinction profile. Each measured profile (also termed "event") gives an along-track separation of ~125 km. The along-track field of view integrates over a distance of ~180 km for each 1 km vertical sample (DeLand and Gorkavyi, 2021).

Atmospheric
Measurement
Techniques
Discussions

Open Access
EGU
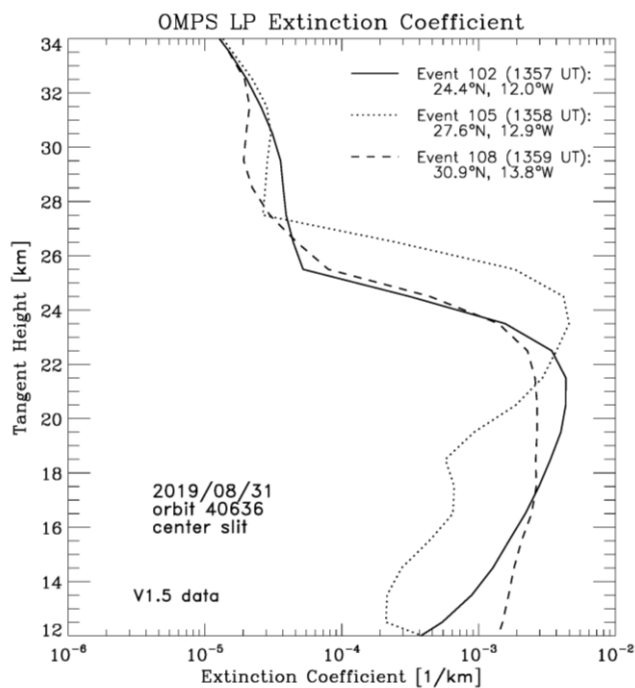
Figure 10: The aerosol formed as a result of the Raikoke eruption is clearly visible in the extinction coefficient
280 **profiles obtained by the OMPS LP aerosol extinction vertical profile months after the eruption.**

3.3 Coherent circular cloud (CCC)

The CCC is part of the original aerosol/SO$_2$ cloud resulting from the eruption of the Raikoke volcano. It formed one month
285 after the eruption in the same area where the volcano is located (Fig. 11). On July 24, 2019, as the CALIOP aerosol data
show, the CCC had a height of 19-20 km and quickly shifted to the south (Fig. 11). On July 30, 2019, it reached a latitude of
30˚N and was extended across China, fell into easterly winds and moved west at about 17 m/s (Fig. 12). On August 4, it was
recorded over the Persian Gulf region, on August 5 - over the Egyptian region, and on August 8 - near the Azores.

290
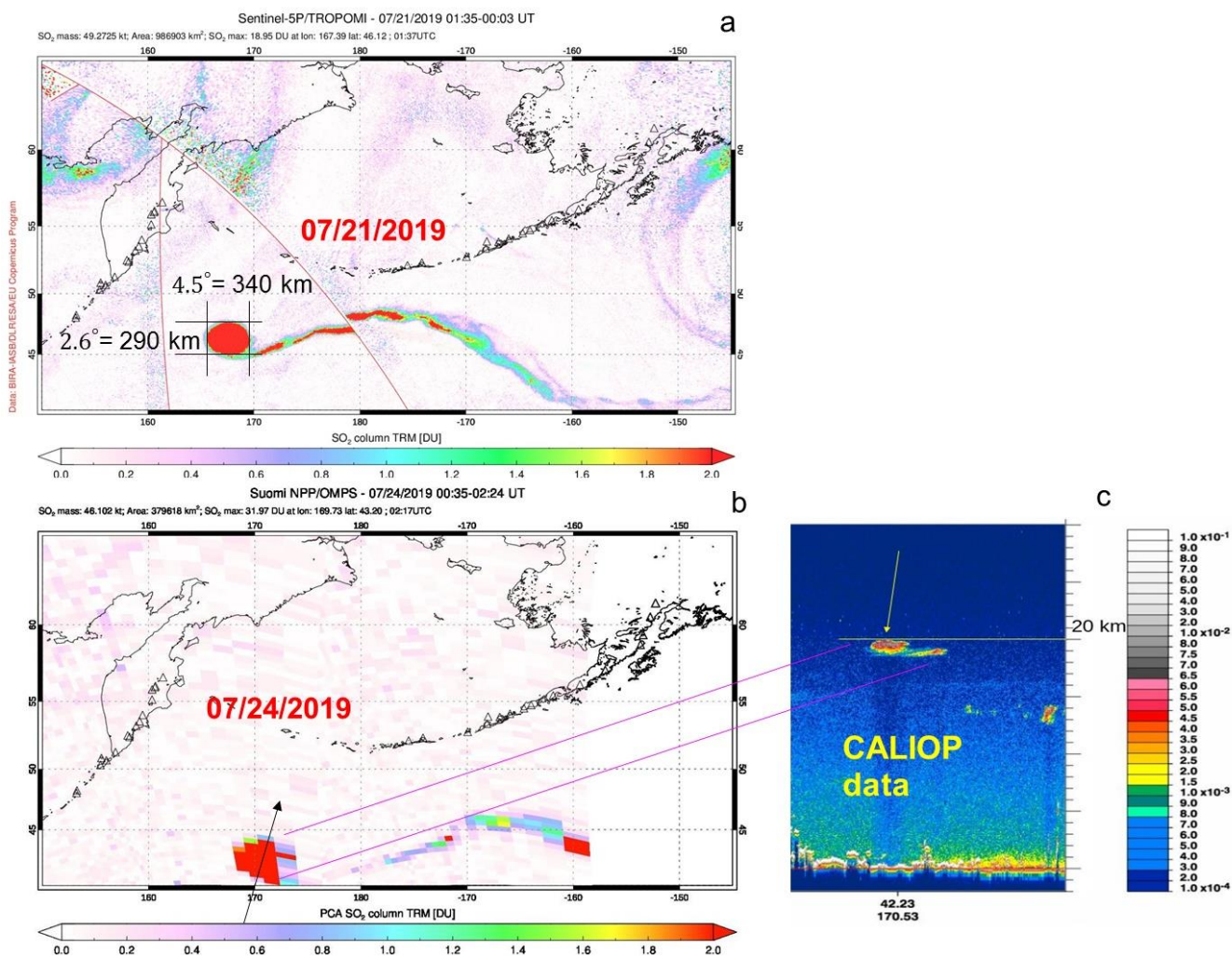
Figure 11: a-b) TROPOMI and OMPS NM SO$_2$ data for 07/21/2019 and 07/24/2019 show the formation of CCC, which appeared near Kamchatka and shifted to latitude ~ 30˚N and moved to west at a speed of 1400 km per day. From OMPS NM data we estimated the initial mass of SO$_2$ in this cloud to be ~20 kt; c) CALIOP total attenuated backscatter data (km^{-1} sr^{-1}) show the height of the CCC to be 18.5-20 km.
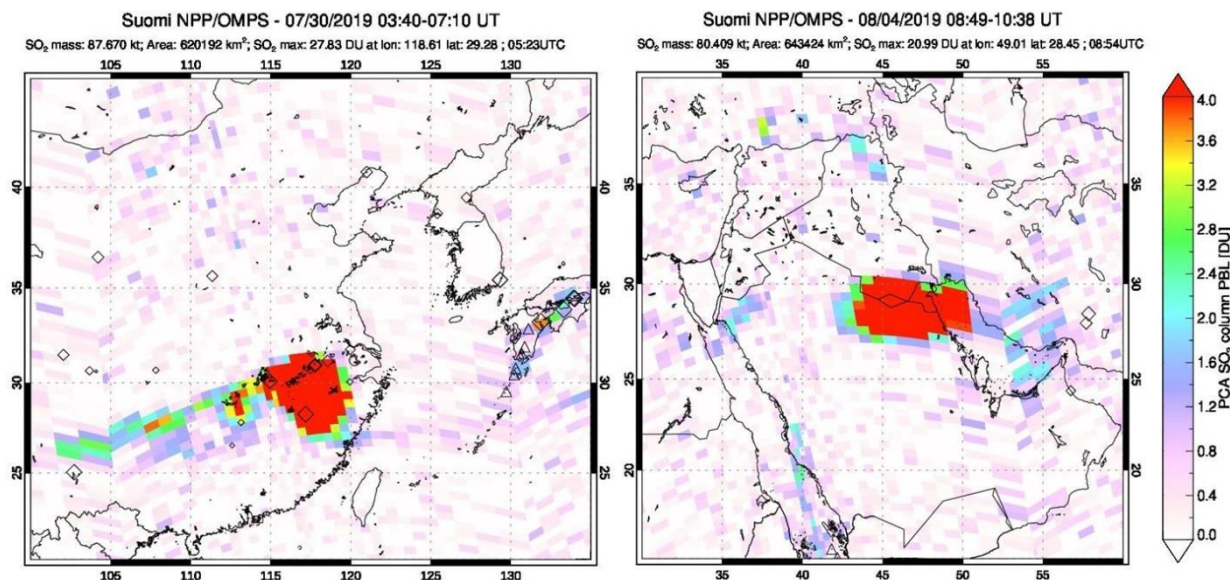
Figure 12: SO$_2$ column data shows the westward drift of the CCC with speed ~ 14-15°/day, ~ 1400 km/day, ~ 60 km/h.

300   The CCC was tracked until the end of August, while making 1.5 orbits around the Earth. CALIOP and OMPS LP (see Fig. 13 with CALIOP data from August 18 and September 1, 2019 and Fig. 4, 10 from August 31, 2019 – OMPS LP data) were able to track the movement of the accompanying aerosol part of this CCC up to September 22 as it made ~ 3 orbits around the Earth.
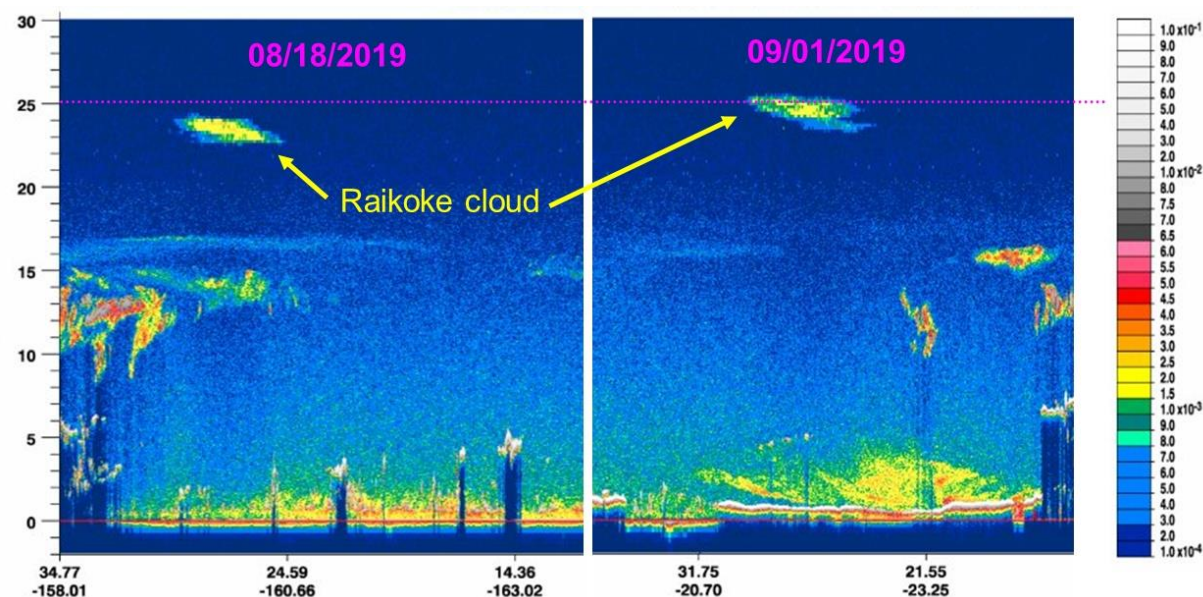

305

Figure 13: The CALIOP total attenuated backscatter data (km^{-1} sr^{-1}) for 08/18 and 09/01/19, where bright aerosol layers are visible at the indicated latitudes and heights show an increase in the height of the layer over time.

15

Figure 14 shows satellite observation of the CCC from July 18 to September 22, 2019. Figure 15 shows the results of
310 backward trajectory modeling of the CCC for one month period with initial days August 18 and September 19, 2019. The basic idea is to use the trajectories to see if this long-lived CCC can be correctly transported using assimilated meteorological observations.
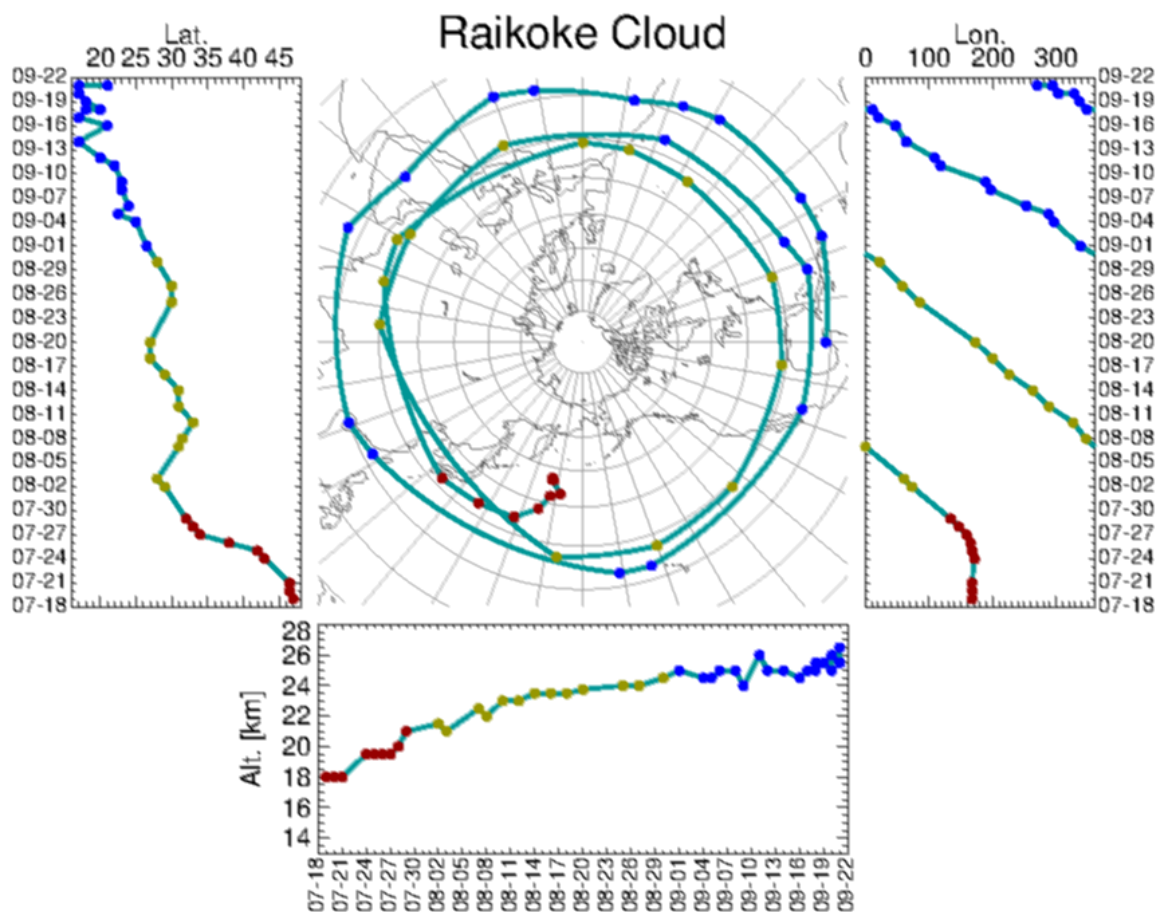
Figure 14: The observed path of the CCC as inferred from OMI/OMPS/TROPOMI and CALIOP observations. The individual observations are shown by dots color-coded by month.

We have two hypotheses to evaluate. The first hypothesis ("the great red spot" hypothesis) is that the observed CCC is contained within a gyre (whirlpool) that existed from around the time of the eruption on June 21 to September 1 or even later, advected around the globe by the large-scale circulation. The second hypothesis (the "dead fish" hypothesis) is that the
320 CCC was simply advected around by the large-scale winds without being sheared apart because the environment of the summer stratosphere is fairly quiescent.

We inspected the meteorological fields from the GMAO GEOS (Rienecker et al., 2008) and from the Global Data Assimilation System (GDAS) by the National Centers for Environmental Prediction (NCEP) at the location and altitude of
325 the observed volcanic CCC on July 21 and 24; the winds show no discernible gyre. This is to be expected, as the satellite data that go into these assimilation products are unlikely to pick up features on sufficiently small scales that they would show up clearly and prominently in the winds. Therefore, it is not possible to test the "great red spot" hypothesis using a trajectory model with the wind products available to us.

16
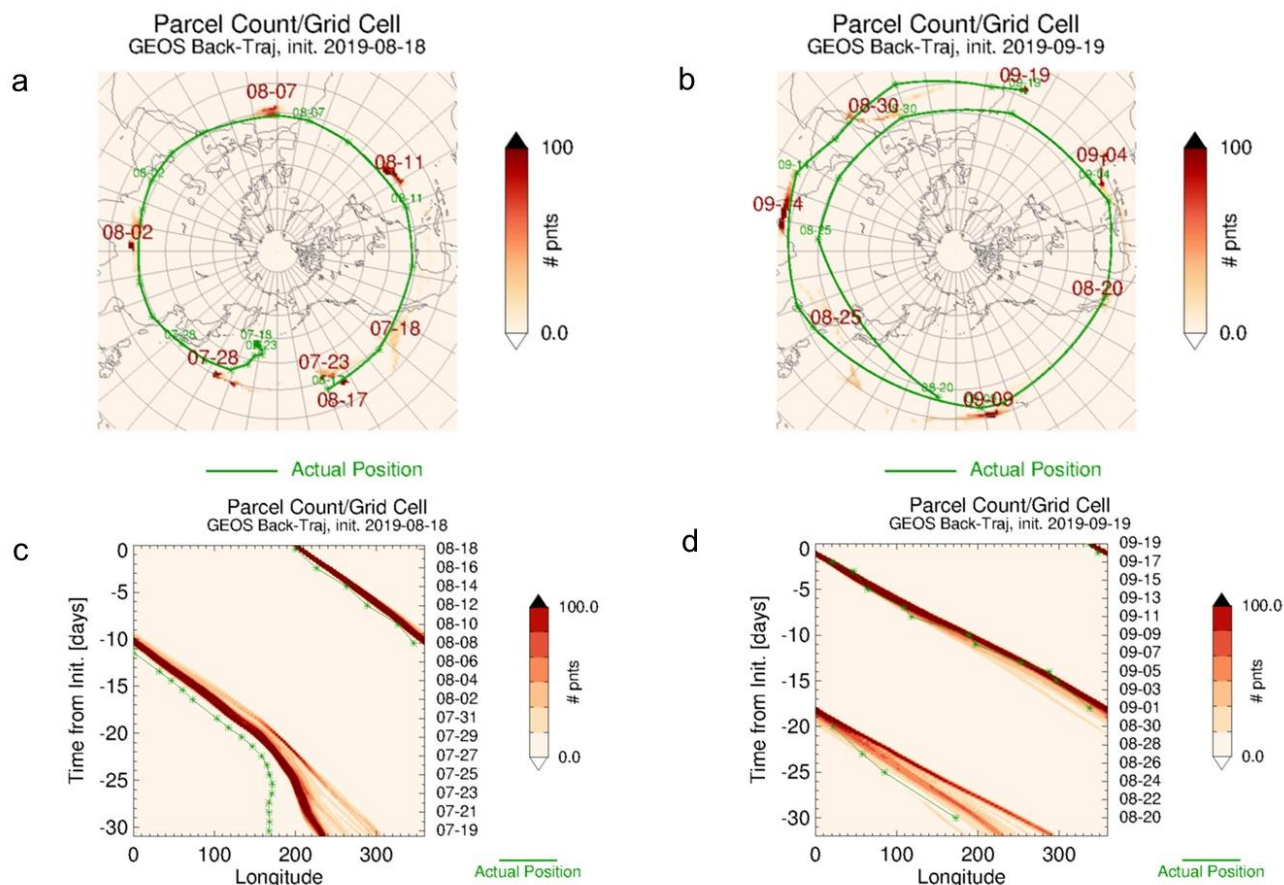
Figure 15: Backward trajectory modeling: a) This panel shows several discrete time snapshots from the Goddard "ftraj" back-trajectory modeling for 3000 parcels within a 150 km radius of the observed CCC position on initialized on 2019-08-18; b) The trajectory model run was initialized with the observed cloud position on 2019-09-19 and then run backwards to 2019-08-18; c) This shows the same model results as for a) but using a different visualization. Here the parcels are binned and counted in longitude and time, regardless of altitude or latitude; d) Similar to c), except that the model run is initialized at 2019-09-19 and ran backwards to 2019-08-18.

We can examine the "dead fish" hypothesis; if a trajectory model run shows a cloud of parcels maintaining its integrity over a long period of time, then this hypothesis becomes plausible. There are difficulties, however. First, the winds used to drive the trajectory model have spatial and temporal resolutions that are coarse enough that trajectories cannot be modelled with perfect accuracy. One can expect that a cloud of parcels will lose many of its parcels along the way. It would be unrealistic to expect to duplicate the volcanic cloud's integrity and position as a function of time. Instead, the test is whether the simulated cloud of parcels can maintain its existence over the course of a month or more during this time period. Second, a more serious problem is that of altitude. We can expect a volcanic CCC to experience self-lofting, and the CCC indeed is observed to increase in altitude with time. However, the winds vary with altitude and thus the parcel trajectories will depend critically on getting their altitude changes right.

Atmospheric
Measurement
Techniques
Discussions

Open Access

EGU

350 A carbonaceous aerosol plume associated with wild fires in British Columbia in August 2017 reached the stratosphere a few days following the initial injection above the tropopause and resulting from self-lofting triggered by solar heating (Torres et al., 2020). The case of a volcanic CCC, which we are considering, is interesting in that the effect of an increase in height from 19 to 26 kilometers is observed for a cloud consisting of sulfate aerosol. In this case, the main increase in the height of the CCC occurred during its movement at approximately the same latitude. Early on (July 19) it is at 80 hPa (450 K), but by September 1 it had risen to 30 hPa (590 K). This is a diabatic self-lofting heating rate of about 3 K per day. Note that this

355 CCC, increasing its height, simultaneously contained a detectable amount of SO_2, which is also confirmed by independent satellite data from ACE (Cameron et al., 2021).

The thermodynamic processes within the cloud are not well-known, so rather than attempting to model the cloud's self-lofting and the overall vertical advection, we impose an approximation to the cloud's vertical motion. We determined an

360 average daily θ adjustment that would map the column of parcels from its initial θ range to its final range. Back-trajectories were then computed isentropically for one day at a time. After each day, the parcels' potential temperature values were changed by their daily adjustment. In this way, the vertical motion of the CCC is guided by observations, while the horizontal motions are unconstrained. Note that this adjustment procedure implies two assumptions: that the self-lofting is linear in time, and that it is linear in θ as well. The map (see Fig.15) displays the parcel population count as a "heat map" or

365 density display: the more intense the color at a given point, the more parcels are near that point (the resolution of the map is $1^{o} \times 1^{o}$). The plot below the map shows a similar "heat map" of parcel population count as a function of longitude (x-axis) and altitude (y-axis); the resolution here is 1° longitude by 0.5 km altitude.

Figure15a superimposes several discrete time snapshots from the trajectory model output, starting with the observed cloud

370 position on 2019-08-18. The modelled positions are generally close to the observed, except that the model fails to pick up the effects of the synoptic weather feature beginning around July 23. Figure15b shows the output from another model run, initialized with the observed CCC position on 2019-09-19 and then run backwards to 2019-08-18. Figure15c,d shows the same model results but using a Hovmueller-type plot.

375 The CCC appears not to be a whirlpool or roll-up, but rather a CCC with easterly flow and drifting ("dead fish" model). Neither the large-scale mixing events nor gravity waves penetrate well into the summer stratosphere to mix features, so they tend to move intact if injected at the right time.

6 Conclusion

We studied the process of converting SO_2 to aerosol. The typical time for SO_2 reduction is 8-10 days, which coincides with

380 the results for Kasatochi (Krotkov et al., 2010). The peak sulfate aerosol is 1.5 months behind the time of maximum release of SO_2. We examined the CCC of SO_2 and aerosol, which was observed for 2.5 months. The CCC is embedded in the summer easterly flow in the stratosphere and demonstrated a diabatic "self-lofting" heating rate of about 3 K per day. For 2.5 months, the CCC circled the globe almost three times at the latitude of $30^{o}N$ and increased its height from 19 to 28 km. The latitudinal distribution of stratospheric optical depth shows that most of the aerosol from Raikoke plume is transported

385 poleward.

The arch effect characteristic of the limb observations should be taken into account when calculating the optical thickness of aerosol clouds, determining a characteristic cloud height or using calibration heights of ~ 45 km, which should be free of aerosol but can be contaminated with polar mesospheric clouds (PMCs) and other high aerosol clouds.

390 **Data availability**

The SO_2 data for OMPS, OMI and TROPOMI data are available at https://so2.gsfc.nasa.gov/ and Goddard Earth Sciences Data and Information Services Center (GES DISC) at

Atmospheric
Measurement
Techniques
Discussions

395 The OMPS-NPP L2 LP Aerosol Extinction Vertical Profile (v1.5) data are available at https://disc.gsfc.nasa.gov/datasets/OMPS_NPP_LP_L2_AER675_DAILY_1.5/summary (Bhartia and Torres, 2019).

Competing interests

The authors declare that they have no conflicts of interest.

Authors's contributions

400 NG, CL, LL, SC, MD, MS, GT developed computer codes and algorithms, analyzed the results and wrote the manuscript. NK, JJ, AV set the task of developing, supported the development of the algorithm, analyzed the results and wrote the manuscript. PN, OT, PC analyzed the data and results and wrote the manuscript.

References

Bhartia, P. K. and Torres, O. O.: OMPS-NPP L2 LP Aerosol Extinction Vertical Profile swath daily 3slit V1.5, Greenbelt,
415 MD, USA, Goddard Earth Sciences Data and Information Services Center (GES DISC), https://doi.org/10.5067/GZJJYA7L0YW2, (last access: 02/25/2021), 2019.

Bluth, G. J. S., Doiron, S. D., Schnetzler, C. C., Krueger, A. J., and Walter, L. S.: Global tracking of the SO$_2$ clouds from the June, 1991 Mount Pinatubo eruptions, Geophys. Res. Lett., 19, 151–154, https://doi.org/10.1029/91GL02792, 1992.
420
Bourassa, A. E., Degenstein, D. A., Elash, B. J., and Llewellyn, E. J.: Evolution of the stratospheric aerosol enhancement following the eruptions of Okmok and Kasatochi: Odin-OSIRIS measurements, J. Geophys. Res.-Atmos., 115, D00L03, https://doi.org/10.1029/2009JD013274, 2010.

425 Bovensmann, H., Burrows, J. P., Buchwitz, M., Frerick, J., Noël, S., Rozanov, V. V., Chance, K. V., and Goede, A. P. H.: SCIAMACHY: Mission objectives and measurement modes, J. Atmos. Sci., 56, 127–150, https://doi.org/10.1175/1520-0469(1999)056<0127:SMOAMM>2.0.CO;2, 1999.

Cameron, W.D., Bernath, P., and Boone, C.: Sulfur dioxide from the atmospheric chemistry experiment (ACE) satellite. J.
430 Quant. Spectrosc. Rad. Trans., 258, 107341, https://doi.org/10.1016/j.jqsrt.2020.107341, 2021.

Carn, S. A., Krueger, A. J., Bluth, G. J. S., Schaefer, S. J., Krotkov, N. A., Watson, I. M., and Datta, S.: Volcanic eruption detection by the Total Ozone Mapping Spectrometer (TOMS) instruments: A 22-year record of sulfur dioxide and ash emissions, Geol. Soc. Spec. Publ., 213, 177–202, https://doi.org/10.1144/GSL.SP.2003.213.01.11, 2003.

435 Carn, S. A., Krueger, A. J., Krotkov, N. A., Yang, K., and Levelt, P. F.: Sulfur dioxide emissions from Peruvian copper smelters detected by the Ozone Monitoring Instrument, Geophys. Res. Lett., 34, L09801, https://doi.org/10.1029/2006GL029020, 2007.

440 Carn, S. A., Krueger, A. J., Arellano, S., Krotkov, N. A., and Yang, K.: Daily monitoring of Ecuadorian volcanic degassing from space, J. Volcanol. Geoth. Res., 176, 141–150, https://doi.org/10.1016/j.jvolgeores.2008.01.029, 2008.

Carn, S. A., Krueger, A. J., Krotkov, N. A., Yang, K., and Evans, K.: Tracking volcanic sulfur dioxide clouds for aviation hazard mitigation, Nat. Hazards, 51, 325–343, https://doi.org/10.1007/s11069-008-9228-4, 2009.

445 Carn, S. A, Fioletov, V. E., McLinden, C. A., Li, C., and Krotkov, N. A.: A decade of global volcanic SO_2 emissions measured from space. Sci. Rep., 7, 44095, https://doi.org/10.1038/srep44095, 2017.

Chen, Z., Bhartia, P. K., Loughman, R., Colarco, P., and DeLand, M.: Improvement of stratospheric aerosol extinction 450 retrieval from OMPS/LP using a new aerosol model, Atmos. Meas. Tech., 11, 6495–6509, https://doi.org/10.5194/amt-11-6495-2018, 2018.

DeLand, M. T. and Gorkavyi, N.: PMC observation from the OMPS Limb Profiler. J. Atmos. Sol.-Terr. Phy., 213, 105505, https://doi.org/10.1016/j.jastp.2020.105505, 2021.

455 Fairlie, T. D., Vernier, J.-P., Natarajan, M., and Bedka, K. M.: Dispersion of the Nabro volcanic plume and its relation to the Asian summer monsoon, Atmos. Chem. Phys., 14, 7045–7057, https://doi.org/10.5194/acp-14-7045-2014, 2014.

Fisher, B. L., Krotkov, N. A., Bhartia, P. K., Li, C., Carn, S. A., Hughes, E., and Leonard, P. J. T.: A new discrete 460 wavelength backscattered ultraviolet algorithm for consistent volcanic SO_2 retrievals from multiple satellite missions, Atmos. Meas. Tech., 12, 5137–5153, https://doi.org/10.5194/amt-12-5137-2019, 2019.

Hedelt, P., Efremenko, D. S., Loyola, D. G., Spurr, R., and Clarisse, L.: Sulfur dioxide layer height retrieval from Sentinel-5 Precursor/TROPOMI using FP_ILM, Atmos. Meas. Tech., 12, 5503-5517, https://doi.org/10.5194/amt-12-5503-2019, 2019.

465 Kloss, C., Berthet, G., Sellitto, P., Ploeger, F., Taha, G., Tidiga, M., Eremenko, M., Bossolasco, A., Jégou, F., Renard, J.-B., and Legras, B.: Stratospheric aerosol layer perturbation caused by the 2019 Raikoke and Ulawun eruptions and their radiative forcing, Atmos. Chem. Phys., 21, 535–560, https://doi.org/10.5194/acp-21-535-2021, 2021.

470 Krotkov, N. A., Schoeberl, M. R., Morris, G. A., Carn, S., and Yang, K.: Dispersion and lifetime of the SO_2 cloud from the August 2008 Kasatochi eruption. J. Geophys. Res.-Atmos., 115, D00L20, https://doi.org/10.1029/2010JD013984, 2010.

Li, C., Joiner, J., Krotkov, N. A., and Bhartia, P. K.: A fast and sensitive new satellite SO_2 retrieval algorithm based on principal component analysis: Application to the ozone monitoring instrument, Geophys. Res. Lett., 40, 6314– 6318, 475 https://doi.org/10.1002/2013GL058134, 2013.

Li, C., Krotkov, N. A., Carn, S., Zhang, Y., Spurr, R. J. D., and Joiner, J.: New-generation NASA Aura Ozone Monitoring Instrument (OMI) volcanic SO_2 dataset: algorithm description, initial results, and continuation with the Suomi-NPP Ozone Mapping and Profiler Suite (OMPS), Atmos. Meas. Tech., 10, 445–458, https://doi.org/10.5194/amt-10-445-2017, 2017.
480

Livesey, N. J., Van Snyder, W., Read, W. G., and Wagner, P. A.: Retrieval algorithms for the EOS Microwave limb sounder (MLS), IEEE T. Geosci. Remote, 44, 1144-1155, https://doi.org/10.1109/TGRS.2006.872327, 2006.

485 Loughman, R., Bhartia, P. K., Chen, Z., Xu, P., Nyaku, E., and Taha, G.: The Ozone Mapping and Profiler Suite (OMPS) Limb Profiler (LP) Version 1 aerosol extinction retrieval algorithm: theoretical basis, Atmos. Meas. Tech., 11, 2633–2651, https://doi.org/10.5194/amt-11-2633-2018, 2018.

Muser, L. O., Hoshyaripour, G. A., Bruckert, J., Horváth, Á., Malinina, E., Wallis, S., Prata, F. J., Rozanov, A., von Savigny, C., Vogel, H., and Vogel, B.: Particle aging and aerosol–radiation interaction affect volcanic plume dispersion: evidence
490 from the Raikoke 2019 eruption, Atmos. Chem. Phys., 20, 15015-15036, https://doi.org/10.5194/acp-20-15015-2020, 2020.

Penning de Vries, M. J. M., Dörner, S., Puķīte, J., Hörmann, C., Fromm, M. D., and Wagner, T.: Characterisation of a stratospheric sulfate plume from the Nabro volcano using a combination of passive satellite measurements in nadir and limb geometry, Atmos. Chem. Phys., 14, 8149–8163, https://doi.org/10.5194/acp-14-8149-2014, 2014.
495

Reinecker, M. M., Suarez, M. J., Todling, R., Bacmeister, J., Takacs, L., Liu, H.-C., Gu, W., Sienkiewicz, M., Koster, R. D., Gelaro, R., Stajner, I., and Nielsen, J. E.: The GEOS-5 Data Assimilation System - Documentation of Versions 5.0.1, 5.1.0, and 5.2.0, Technical Report Series on Global Modeling and Data Assimilation, 27. Ed. M.J. Suarez, NASA/TM–2008– 104606, NASA, Greenbelt, MD, https://gmao.gsfc.nasa.gov/pubs/docs/Rienecker369.pdf, (last access: 02/25/2021), 2008.
500

Sandvik, O. S., Friberg, J., Martinsson, B. G., van Velthoven, P. F. J., Hermann, M., and Zahn, A.: Intercomparison of *in-situ* aircraft and satellite aerosol measurements in the stratosphere, Sci. Rep.-UK, 9, 15576, https://doi.org/10.1038/s41598-019-52089-6, 2019.

505 von Savigny, C., Timmreck, C., Buehler, S. A., Burrows, J. P., Giorgetta, M., Hegerl, G., Horvath, A., Hoshyaripour, G. A., Hoose, C., Quaas, J., Malinina, E., Rozanov, A., Schmidt, H., Thomason, L., Toohey, M., and Vogel, B.: The Research Unit VolImpact: Revisiting the volcanic impact on atmosphere and climate – preparations for the next big volcanic eruption, Meteorol. Z., 29, 3-18, https://doi.org/10.1127/metz/2019/0999, 2020.

510 Schoeberl, M., and Sparling, L. C.: Trajectory modeling. In "Diagnostic Tools in Atmospheric Physics", Eds G. Fiocco and G. Visconti, Proc. Int. Sch. Phys. Enrico Fermi, 124, 289 – 305, 1995.

Toohey, M., Krüger, K., Schmidt, H., Timmreck, C., Sigl, M., Stoffel, M., and Wilson, R.: Disproportionately strong climate forcing from extratropical explosive volcanic eruptions, Nat. Geosci., 12, 100-107, https://doi.org/10.1038/s41561-018-
515 0286-2, 2019.

Torres, O., Bhartia, P. K., Taha, G., Jethva, H., Das, S., Colarco, P., Krotkov, N., Omar, A., and Ahn, C.: Stratospheric injection of massive smoke plume from Canadian boreal fires in 2017 as seen by DSCOVR-EPIC, CALIOP, and OMPS-LP observations, J. Geophys. Res.-Atmos., 125, e2020JD032579, https://doi.org/10.1029/2020JD032579, 2020.
520

Theys, N., De Smedt, I., Yu, H., Danckaert, T., van Gent, J., Hörmann, C., Wagner, T., Hedelt, P., Bauer, H., Romahn, F., Pedergnana, M., Loyola, D., and Van Roozendael, M.: Sulfur dioxide retrievals from TROPOMI onboard Sentinel-5 Precursor: algorithm theoretical basis, Atmos. Meas. Tech., 10, 119–153, https://doi.org/10.5194/amt-10-119-2017, 2017.

525 Theys, N., Hedelt, P., De Smedt, I., Lerot, C., Yu, H., Vlietinck, J., Pedergnana, M., Arellano, S., Galle, B., Fernandez, G., Carlito, C. J. M., Barrington, C., Taisne, B., Delgado-Granados, H., Loyola, G., and Van Roozendael, M.: Global monitoring of volcanic SO$_2$ degassing with unprecedented resolution from TROPOMI onboard Sentinel-5 Precursor, Sci. Rep.-UK, 9, 2643, https://doi.org/10.1038/s41598-019-39279-y, 2019.

21

530   Zawada, D. J., Rieger, L. A., Bourassa, A. E., and Degenstein, D. A.: Tomographic retrievals of ozone with the OMPS Limb Profiler: algorithm description and preliminary results, Atmos. Meas. Tech., 11, 2375–2393, https://doi.org/10.5194/amt-11-2375-2018, 2018.

Zhang, Y., Li, C., Krotkov, N. A., Joiner, J., Fioletov, V., and McLinden, C.: Continuation of long-term global SO_2 pollution
535   monitoring from OMI to OMPS, Atmos. Meas. Tech., 10, 1495–1509, https://doi.org/10.5194/amt-10-1495-2017, 2017.